Multiparametric Electromagnetic Inversion of 3-D Biaxial Anisotropic Objects Embedded in Layered Uniaxial Media Using VBIM Enhanced by Structural Consistency Constraint

Jianliang Zhuo, Longfang Ye, Feng Han, *Member, IEEE*, Liujing Xiong, and Qing Huo Liu, *Fellow, IEEE*

***Abstract*— This article presents the 3-D inversion of biaxial anisotropic objects embedded in layered uniaxial media by the variational Born iterative method (VBIM). Although previously only the isotropic complex permittivity profile was reconstructed, here we retrieve all the six diagonal anisotropic permittivity and conductivity parameters simultaneously. In the forward model, the stabilized biconjugate gradient fast Fourier transform (BCGS-FFT) method is used to solve the volume electric field integral equation (EFIE). In the inversion model, VBIM is employed to minimize the cost function. In order to improve the inversion results, we propose a novel structural consistency constraint (SCC) applied to VBIM. The SCC is based on the Monte Carlo method and reduces the computational domain in the Born iteration. The major new contribution of this work is to combine the deterministic inversion algorithm VBIM with the stochastic Monte Carlo method to reconstruct all the diagonal anisotropic parameters of the scatterers. Several typical numerical models are simulated, and the results validate the efficiency, antinoise ability as well as the accuracy of VBIM-SCC for reconstructing 3-D biaxial anisotropic objects embedded in multilayered uniaxial media.**

***Index Terms*— Biaxial anisotropic, layered uniaxial media, Monte Carlo method, structural consistency constraint (SCC), variational Born iterative method (VBIM).**

I. Introduction

ELECTROMAGNETIC (EM) inversion uses the measured EM fields scattered by the unknown objects embedded in a region of interest to infer their structures and/or dielectric parameters. Various EM inversion techniques are widely adopted in civilian as well as military applications [1]–[5]. Most inversion is carried out in an isotropic background medium. However, in many geophysical exploration scenarios such as down-hole well-logging [6], magnetotellurics [7], and hydraulic fracture mapping [8], the anisotropy of the background media must be taken into account. One common model is the transverse isotropy (or uniaxial anisotropy). Therefore, it is desirable to develop an anisotropic EM inversion algorithm for scatterers embedded in layered uniaxial media and explore its potential applications.

Since inverse scattering problems are usually nonlinear and ill-posed, the accuracy, stability, and efficiency are three core topics in EM inversion. To address these issues, researchers have done lots of research for different solutions and achieved good results. The inverse problems are solved either by the linear approximation methods [9]–[11] or by nonlinear iterative methods. Due to the multiple scattering among scatterers, a linear method works only for a weak EM scattering scenario. Several nonlinear iterative methods have been developed to deal with the strong scattering scenario. One method is to transform the nonlinear relationship between the scattered field and the model dielectric parameters into an optimization problem, such as the contrast source inversion (CSI) [12]–[14] and subspace-based optimization method (SOM) [15]–[17]. These kinds of methods generally require good initial values [18].

Another nonlinear iterative method requires forward computation in each iteration. The total electric field in the inversion domain is updated in the forward computation by assuming the model parameters are known. In the inversion, the model parameters are updated by minimizing the difference (misfit) between the measured and simulated scattered field based on the reconstructed parameters. The initial values of model parameters are guessed to start the iteration. This kind of methods includes the Born iterative method (BIM) [2], [19], distorted BIM (DBIM) [20]–[23], and variational BIM (VBIM) [1], [24], [25]. Once the total fields are updated by the forward solver, iterative methods such as conjugate gradient (CG) [26] or Gauss–Newton inversion (GNI) [27] can be used to find the optimized model parameters. BIM was first developed by Wang and Chew [19] to reconstruct the 2-D permittivity profile of an inhomogeneous medium. They then proposed the DBIM [20] which has a faster convergence speed than

Manuscript received June 17, 2019; revised December 1, 2019; accepted January 12, 2020. Date of publication February 3, 2020; date of current version June 2, 2020. This work was supported by the National Key Research and Development Program of the Ministry of Science and Technology of China under Grant 2018YFC0603503 and Grant 2018YFF01013300. *(Corresponding authors: Feng Han; Qing Huo Liu.)*

Jianliang Zhuo is with the Postdoctoral Mobile Station of Information and Communication Engineering, Key Laboratory of Electromagnetic Wave Science and Detection Technology, Xiamen University, Xiamen 361005, China.

Longfang Ye, Feng Han, and Liujing Xiong are with the Key Laboratory of Electromagnetic Wave Science and Detection Technology, Institute of Electromagnetics and Acoustics, Xiamen University, Xiamen 361005, China (e-mail: feng.han@xmu.edu.cn).

Qing Huo Liu is with the Department of Electrical and Computer Engineering, Duke University, Durham, NC 27708 USA (e-mail: qhliu@duke.edu).

Color versions of one or more of the figures in this article are available online at http://ieeexplore.ieee.org.

Digital Object Identifier 10.1109/TAP.2020.2969976

BIM although the stability of the iterative process is not as good as that of the BIM. The DBIM method is later widely used in inversion problems. For example, Yu *et al*. [22] used the DBIM to perform image reconstruction of 3-D dielectric targets from multifrequency experimental data. To avoid repetitive computation of the Green's function in each iteration of the DBIM, Nie *et al*. [24] developed the 2-D VBIM which can be switched to BIM conveniently. Zhang and Liu [25] developed the VBIM in the simultaneous reconstruction of permittivity and permeability contrasts in 3-D isotropic media. Due to the faster convergence compared with the BIM and less computation cost compared with DBIM, the VBIM is employed in this article.

There are several previous research works related to the anisotropic inversion. For example, the anisotropic conductivity in each layer was retrieved in [7]. The inversion of 2-D uniaxial anisotropic scatterers embedded in homogeneous background media by the SOM was given in [16] and [17]. Inversion for multiple small anisotropic spheres by the multiple signal classification (MUSIC) method was presented in [28]. In this article, we present the first multiparameteric inversion of 3-D biaxial anisotropic dielectric objects embedded in layered uniaxial media by VBIM. The optical axes of both the scatterers and the background medium are assumed perpendicular to the layer interface. Meanwhile, the scatterers and the background medium are nonmagnetic and lossy, and thus, there are totally six parameters to be reconstructed for both the permittivity and conductivity. Uniquely solving for so many parameters is a challenging task. Noting that these six parameters usually share the same geometry structure, we develop a structural consistency constraint (SCC) algorithm based on the Monte Carlo method to reduce the inversion domain as well as the unknowns in the nonlinear inversion iteration. In order to simultaneously invert for permittivity and conductivity, we formulate the inversion data equation by combining the real and imaginary parts together to form a pure real equation, and the frequency information is integrated into the Fréchet derivative matrix. Accordingly, the real and imaginary parts of multifrequency scattered field data are also separated and reunited to form the measured field vector. The real form inversion data equations are solved by VBIM with the SCC. And the 3-D biaxial anisotropic dielectric objects are reconstructed.

The organization of this article is as follows. In Section II, the detailed description of the theory is presented. In the forward model, the scattered field and the total field are calculated for known dielectric model parameters using the biconjugate gradient fast Fourier transform (BCGS-FFT) method. In the inversion model, the inversion data equations in real forms are solved by VBIM. Finally, the SCC algorithm is discussed in detail. In Section III, three numerical models are simulated. In the first model, the inversion results as well as computation efficiency are compared for the VBIM with and without SCC applied. In the following two models, irregular as well as multiple objects are reconstructed by the proposed VBIM-SCC algorithm when the noise of different levels is added to the synthetic data. In Section IV, conclusions are drawn.

II. Methods

The objective of this article is to invert for the 3-D biaxial anisotropic objects completely embedded in the mth uniaxial medium layer with the optical axis in the z-direction. The objects are not allowed to be placed across layer boundaries. The typical configuration of scattering and inverse scattering can be referred to Fig. 1 in [29] and [30]. Each layer of the background medium has independent permittivity and conductivity but the same permeability as that of free space μ_0. The relative permittivity and conductivity tensors of the ith layer are written as

$$\overline{\overline{\varepsilon}}_b^i = \mathrm{diag}\{\varepsilon_{xb}^i, \varepsilon_{xb}^i, \varepsilon_{zb}^i\}, \quad \overline{\overline{\sigma}}_b^i = \mathrm{diag}\{\sigma_{xb}^i, \sigma_{xb}^i, \sigma_{zb}^i\} \tag{1}$$

where the subscript b denotes the background. The relative complex permittivity tensor of the ith layer is expressed as

$$\overline{\overline{\epsilon}}_b^i = \overline{\overline{\varepsilon}}_b^i + \frac{\overline{\overline{\sigma}}_b^i}{j\omega\varepsilon_0}. \tag{2}$$

The relative permittivity and conductivity tensors of the scatterer are written as

$$\overline{\overline{\varepsilon}}_s = \mathrm{diag}\{\varepsilon_{xs}, \varepsilon_{ys}, \varepsilon_{zs}\}, \quad \overline{\overline{\sigma}}_s = \mathrm{diag}\{\sigma_{xs}, \sigma_{ys}, \sigma_{zs}\}. \tag{3}$$

The relative complex tensor permittivity of the scatterer is defined as

$$\overline{\overline{\epsilon}}_s = \overline{\overline{\varepsilon}}_s + \frac{\overline{\overline{\sigma}}_s}{j\omega\varepsilon_0} \tag{4}$$

where ω is the operating angular frequency. The six parameters in (3) are reconstructed in this article.

A. Forward Model

According to the EM scattering theory [31], [32], the scattered electric field $\mathbf{E}_{\mathrm{sct}}$ and magnetic field $\mathbf{H}_{\mathrm{sct}}$ are equal to the fields radiated by the unknown equivalent electric current source $\mathbf{J}_{\mathrm{eq}}$

$$\mathbf{J}_{\mathrm{eq}}(\mathbf{r}) = j\omega\varepsilon_0(\overline{\overline{\epsilon}}_s(\mathbf{r}) - \overline{\overline{\epsilon}}_b^m)\mathbf{E}_{\mathrm{tot}}(\mathbf{r}) \tag{5}$$

in the background medium where $\mathbf{r}$ is the position vector in the 3-D space. $\mathbf{E}_{\mathrm{tot}}$ is the total field inside the object embedded in the mth layer, and it is obtained by solving the volume electric field integral equation (EFIE) [30], [33]

$$\mathbf{E}_{\mathrm{tot}}(\mathbf{r}) = \mathbf{E}_{\mathrm{inc}}(\mathbf{r}) - j\omega\left(\mathbf{I} + \frac{1}{k_0^2\epsilon_{xb}^m}\nabla\nabla\cdot\right)\mathbf{A}^m(\mathbf{r}) \tag{6}$$

where the superscript m stands for the mth layer, $k_0 = \omega\sqrt{\varepsilon_0\mu_0}$ is the wavenumber in the free space, and $\mathbf{A}$ is the magnetic vector potential in the layered uniaxial medium [33]. The discretized matrix form of (6) is solved by the BCGS-FFT method, and the details can be found in [30]. The scattered electric field $\mathbf{E}_{\mathrm{sct}}$ and magnetic field $\mathbf{H}_{\mathrm{sct}}$ can be written as

$$\mathbf{E}_{\mathrm{sct}}(\mathbf{r}) = j\omega\varepsilon_0 \int \overline{\overline{\mathbf{G}}}_{\mathbf{EJ}}^m(\mathbf{r}, \mathbf{r}')(\overline{\overline{\epsilon}}_s(\mathbf{r}') - \overline{\overline{\epsilon}}_b^m)\mathbf{E}_{\mathrm{tot}}(\mathbf{r}')d\mathbf{r}' \tag{7}$$

$$\mathbf{H}_{\mathrm{sct}}(\mathbf{r}) = j\omega\varepsilon_0 \int \overline{\overline{\mathbf{G}}}_{\mathbf{HJ}}^m(\mathbf{r}, \mathbf{r}')(\overline{\overline{\epsilon}}_s(\mathbf{r}') - \overline{\overline{\epsilon}}_b^m)\mathbf{E}_{\mathrm{tot}}(\mathbf{r}')d\mathbf{r}' \tag{8}$$

where $\overline{\overline{\mathbf{G}}}_{\mathbf{EJ}}^m$ and $\overline{\overline{\mathbf{G}}}_{\mathbf{HJ}}^m$ are, respectively, the mth layer dyadic Green's functions for the electric field and magnetic field in

the layered uniaxial medium and can be found in [33]. They include the contributions from the direct EM wave propagation from the source and those from the multiple reflected and transmitted EM waves in the layer boundaries. This makes the inverse scattering problem in multilayered media considerably more complicated than that in a homogeneous background.

In the forward problem, the scatterer parameter $\overline{\overline{\epsilon}}_s$ is known, and $\mathbf{E}_{\text{tot}}$ is solved from EFIE (6) by the BCGS-FFT, and integrals in (7) and (8) are performed to obtain the $\mathbf{E}_{\text{sct}}$ and $\mathbf{H}_{\text{sct}}$.

B. Inversion Model

In the inversion model, the scattered fields $\mathbf{E}_{\text{sct}}$ and $\mathbf{H}_{\text{sct}}$ can be measured at some discrete locations and the tensor $\overline{\overline{\epsilon}}_s$ is the unknown to be solved. We assume that M_T transmitters, M_R receivers, and M_F operation frequencies are used to collect the scattered fields. The rectangular inversion domain is divided into $N = N_x \times N_y \times N_z$ cells, and each cell has six unknowns (ε_{xs}, ε_{ys}, ε_{zs}, σ_{xs}, σ_{ys}, and σ_{zs}) to be solved for the biaxial objects. So, the total unknown number is 6 N. By virtue of (7) and (8), the data equation with the unknown $\overline{\overline{\epsilon}}_s$ for the ith frequency can be discretized as

$$\mathbf{L}'(\omega_i) = \mathbf{A}'(\omega_i)\mathbf{x}(\omega_i) \tag{9}$$

where ω_i is the ith angular frequency. $\mathbf{L}'(\omega_i)$ is a 6 $M_T M_R$ column vector containing the measured scattered data whose column elements are expressed as

$$\mathbf{L}'(\omega_i) = \begin{bmatrix} \mathbf{E}_{\text{sct}}(\mathbf{r}_{iR}, \mathbf{r}_{iT}, \omega_i) \\ \eta_0 \mathbf{H}_{\text{sct}}(\mathbf{r}_{iR}, \mathbf{r}_{iT}, \omega_i) \end{bmatrix}. \tag{10}$$

Here, η_0 is the intrinsic impedance of air, and $\mathbf{A}'(\omega_i)\mathbf{x}(\omega_i)$ represents the reconstructed scattered field. $\mathbf{A}'(\omega_i)$ is a 6 $M_T M_R \times 3N$ matrix, whose elements for the kth cell are given as

$$\mathbf{A}'(\omega_i) = j\omega_i \varepsilon_0 \Delta V \begin{bmatrix} \overline{\overline{\mathbf{G}}}^m_{\mathbf{EJ}}(\mathbf{r}_{iR}, \mathbf{r}'_k, \omega_i) \\ \eta_0 \overline{\overline{\mathbf{G}}}^m_{\mathbf{HJ}}(\mathbf{r}_{iR}, \mathbf{r}'_k, \omega_i) \end{bmatrix} \mathbf{E}_{\text{tot}}(\mathbf{r}'_k, \mathbf{r}_{iT}, \omega_i). \tag{11}$$

The $\mathbf{x}(\omega_i)$ is the unknown to be solved for biaxial objects, whose elements for each cell are given as

$$\mathbf{x}(\omega_i) = \begin{bmatrix} (\varepsilon_{xs} - \varepsilon^m_{xb}) + \dfrac{1}{j\omega_i\varepsilon_0}(\sigma_{xs} - \sigma^m_{xb}) \\ (\varepsilon_{ys} - \varepsilon^m_{xb}) + \dfrac{1}{j\omega_i\varepsilon_0}(\sigma_{ys} - \sigma^m_{xb}) \\ (\varepsilon_{zs} - \varepsilon^m_{zb}) + \dfrac{1}{j\omega_i\varepsilon_0}(\sigma_{zs} - \sigma^m_{zb}) \end{bmatrix}. \tag{12}$$

Obviously, the unknown $\mathbf{x}(\omega_i)$ is different for different operation frequencies. Therefore, the data equation (9) is reformulated as the real equation with the same unknown for all operation frequencies, whose expression is rewritten as

$$\mathbf{L} = \mathbf{A}\mathbf{y} \tag{13}$$

where $\mathbf{L}$ is the combination of the real and imaginary parts of the measured fields for all operation frequencies. And the total number of elements in $\mathbf{L}$ is $M = 12M_T M_R M_F$. It is evaluated by

$$\mathbf{L}(\omega_i) = \begin{bmatrix} \text{Re}(\mathbf{L}'(\omega_i)) \\ \text{Im}(\mathbf{L}'(\omega_i)) \end{bmatrix} \tag{14}$$

for the ith frequency. $\mathbf{A}$ is an $M \times 6N$ matrix, whose elements for each frequency are

$$\mathbf{A}(\omega_i) = \begin{bmatrix} \text{Re}(\mathbf{A}'(\omega_i)) & \dfrac{\text{Im}(\mathbf{A}'(\omega_i))}{\omega_i\varepsilon_0} \\ \text{Im}(\mathbf{A}'(\omega_i)) & -\dfrac{\text{Re}(\mathbf{A}'(\omega_i))}{\omega_i\varepsilon_0} \end{bmatrix}. \tag{15}$$

The vector $\mathbf{y}$ has $6N$ unknowns, whose elements for each cell are

$$\mathbf{y} = \left[\varepsilon_{xs} - \varepsilon^m_{xb}, \varepsilon_{ys} - \varepsilon^m_{xb}, \varepsilon_{zs} - \varepsilon^m_{zb}, \sigma_{xs} - \sigma^m_{xb}, \sigma_{ys} - \sigma^m_{xb}, \sigma_{zs} - \sigma^m_{zb}\right]^T \tag{16}$$

where T denotes the matrix transpose. In order to solve the data equation (13) by VBIM, we normalize the elements of (16) by the corresponding background parameters to ensure that they have the same order of magnitude. The new form of $\mathbf{y}$ is the contrast and is given as

$$\mathbf{y}' = \left[\varepsilon_{xs}/\varepsilon^m_{xb} - 1, \varepsilon_{ys}/\varepsilon^m_{xb} - 1, \varepsilon_{zs}/\varepsilon^m_{zb} - 1, \sigma_{xs}/\sigma^m_{xb} - 1, \sigma_{ys}/\sigma^m_{xb} - 1, \sigma_{zs}/\sigma^m_{zb} - 1\right]^T. \tag{17}$$

The matrix $\mathbf{A}$ is modified accordingly and denoted as $\mathbf{B}$ to keep the data equation (13) correct. By taking the variation of the data equation (13) with respect to $\mathbf{y}'$, we obtain

$$\delta\mathbf{L}_n \cong \mathbf{B}_n \delta\mathbf{y}'_n \tag{18}$$

where $\delta\mathbf{L}_n$ is the difference between the measured data and the reconstructed data in the nth iteration. $\mathbf{B}_n$ can be acquired from (11) and (15). As the initial value of unknown $\mathbf{y}'$, $\mathbf{y}'_0$ is set to zero. And $\delta\mathbf{y}'_{n+1}$ at the $(n+1)$th iteration is defined as

$$\delta\mathbf{y}'_{n+1} = \mathbf{y}'_{n+1} - \mathbf{y}'_n. \tag{19}$$

The cost function with the regularization term in the $(n+1)$th iteration step is defined as

$$F(\delta\mathbf{y}'_{n+1}) = \frac{\|\delta\mathbf{L}_n - \mathbf{B}_n\delta\mathbf{y}'_{n+1}\|^2}{\|\delta\mathbf{L}_n\|^2} + \gamma^2 \frac{\|\delta\mathbf{y}'_{n+1}\|^2}{\|\delta\mathbf{y}'_n\|^2} \tag{20}$$

where γ is the regularization factor. $\|\cdot\|$ is the L_2 norm and $\|\delta\mathbf{y}'_{n+1}\|^2/\|\delta\mathbf{y}'_n\|^2$ is a self-adapting regularization coefficient which can make the process of inversion more stable [1]. The minimization of the cost function is equivalent to solving the following equation [34]:

$$\left(\mathbf{B}_n^T\mathbf{B}_n + \gamma^2 \frac{\|\delta\mathbf{L}_n\|^2}{\|\delta\mathbf{y}'_n\|^2}\mathbf{I}\right)\delta\mathbf{y}'_{n+1} = \mathbf{B}_n^T\delta\mathbf{L}_n. \tag{21}$$

This equation can be efficiently solved by the CG method [35]. In addition, in the iteration process, a nonlinear transform is used to constrain the reconstructed parameters within a reasonable range to avoid nonphysical values [2], [36].

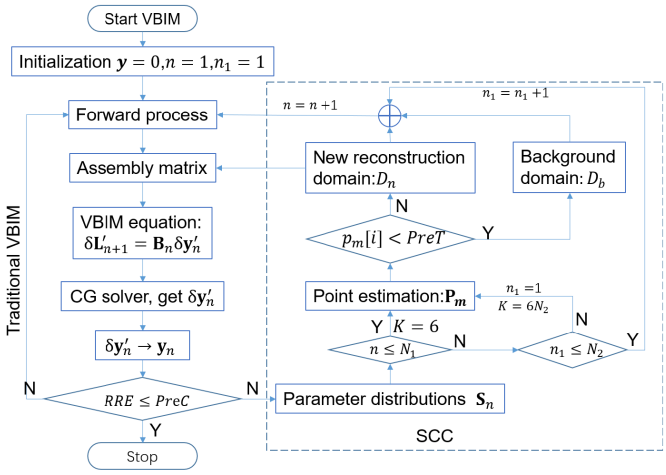

Fig. 1. Flowchart of the VBIM without and with SCC based on Monte Carlo method.

C. SCC Algorithm Based on the Monte Carlo Method

Because the unknown geometry structures of the scatterers usually do not occupy the whole inversion domain, the reconstruction region can be decomposed into scatterer subregions and the remaining background subregion. The dielectric parameters of the background subregion are known. Therefore, the unknowns in this subregion are redundant for the solution of (21) since they have no contribution to the scattered field. If the discretized cells for these redundant unknowns can be effectively removed, the inversion domain may be compressed as small as the scatterers. This can improve the accuracy of the reconstructed parameters and save CPU time and computer memory. Therefore, we develop the SCC algorithm based on the Monte Carlo method to determine whether a certain discretized cell in the inversion domain is the "background" or the "scatterer." If it is judged as the "background," the unknowns for this cell will be discarded in the next VBIM iteration.

Solving an inverse problem is using some measurements of the observable parameters to infer the true values of model parameters, which provide the parameter distribution over the inversion space [37]. Due to the restriction of the data equation (21), the reconstructed parameters are pseudorandom. Six model parameters are obtained after each iteration and different parameters in a discretized cell probably show different structures ("background" or "scatterer"), although the ground truth is that they usually share the same structure. Now let us assume the structure in each cell obeys the Bernoulli distribution (0 for "background," 1 for "scatterer"). Six reconstructed parameters are six samples. We adopt the Monte Carlo method and the point estimation, i.e., use the sample mean value to replace the probability of the "scatterer." If this probability is smaller than a prescribed threshold, the cell structure is treated as "background." The unknowns in this cell and the corresponding columns in the matrix $\mathbf{B}_n$ in (18) will be removed in the next iteration.

The flowchart of the VBIM with and without SCC is shown in Fig. 1. The left panel is the traditional VBIM algorithm given in [24]. The RRE denotes the relative residual error between the measured scattered data and the calculated scattered data

$$\mathrm{RRE}=\frac{\|\mathbf{L}-\mathbf{L}_n\|}{\|\mathbf{L}\|}. \tag{22}$$

$PreC$ in Fig. 1 denotes the prescribed threshold for the stop condition of VBIM. The flowchart in the dotted box is the SCC algorithm which is composed of two parts. The structure distribution is obtained by normalizing the reconstructed parameters $\mathbf{y}_n$ for each cell, and it is defined as

$$\mathbf{s}_n[k]=\frac{\mathrm{abs}(\mathbf{y}_n[k])}{\max(\mathrm{abs}(\mathbf{y}_n[k])} \tag{23}$$

for the kth retrieved parameter (sample) in the nth iteration. The max in the denominator represents the maximum value in all the discretized cells. In virtue of the definition of $\mathbf{y}_n$ in (16), $\mathbf{s}_n$ can be treated as the probability of "scatterer" of a certain discretized cell. As shown in Fig. 1, in the first part, only six samples in each iteration are used for the point estimation for the first N_1 iterations. This can preliminarily determine the locations and sizes of the objects and remove the most redundant background cells. In the second part, the point estimation is performed after every N_2 iterations. And the samples are increased to $6N_2$ to improve the accuracy of the point estimation. The sample space for the mth point estimation is denoted as $\mathbf{S}_m$ with the size of K. Therefore, the probability of "scatterer" for the mth point estimation $\mathbf{P}_m$ is calculated by the arithmetic mean of $\mathbf{S}_m$

$$\mathbf{P}_m=\frac{\sum_{k=1}^{K}\mathbf{S}_m}{K},\quad \mathbf{S}_m=\begin{cases}\mathbf{s}_n[k], & m\le N_1\\ \sum_{n_1=1}^{N_2}\mathbf{s}_{n+n_1}[k], & m>N_1.\end{cases} \tag{24}$$

In Fig. 1, $p_m[i]$ is the element of $\mathbf{P}_m$ for the ith cell. $PreT$ is the prescribed threshold for the point estimation. D_n denotes the new inversion domain for the next iteration in which the parameters are not changed. D_b denotes the remaining domain in which all the cells are mandatorily set as "background." D_n and D_b together form the whole inversion domain. In the next iteration, the total field $\mathbf{E}_{\mathrm{tot}}$ is obtained for the whole inversion domain, but the Fréchet derivative matrix is assembled only for D_n.

From the above discussions, we know that the SCC algorithm is implemented after each VBIM iteration or several VBIM iterations and only used to reconstruct the structures of the objects. The implementation is the statistical processing of results from the CG solver. Although we only combine the SCC with VBIM in this article, it not only works for VBIM. Actually, it can be easily combined with any voxel-based deterministic inversion algorithms such as SOM or CSI as long as the sampling space is large enough.

III. Numerical Results

In this section, three numerical models are used to demonstrate the effectiveness of the inversion method. The first case is only for methodological validation, and the other two cases are implemented to mimic the actual applications of through-the-wall imaging and cross-well measurements, respectively.

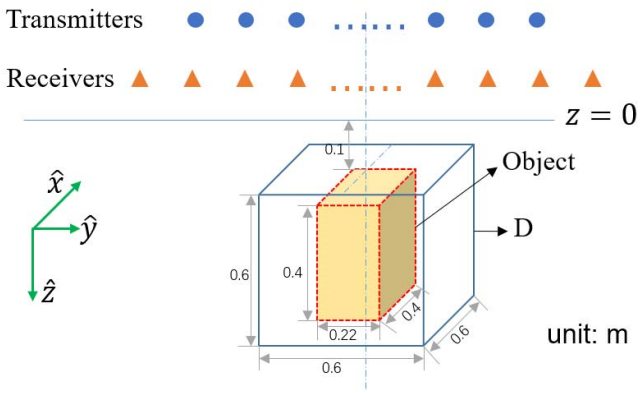

Fig. 2. Configuration of the inversion model with a cuboid scatterer with the dimensions of 0.4 m × 0.22 m × 0.4 m embedded in the bottom layer.

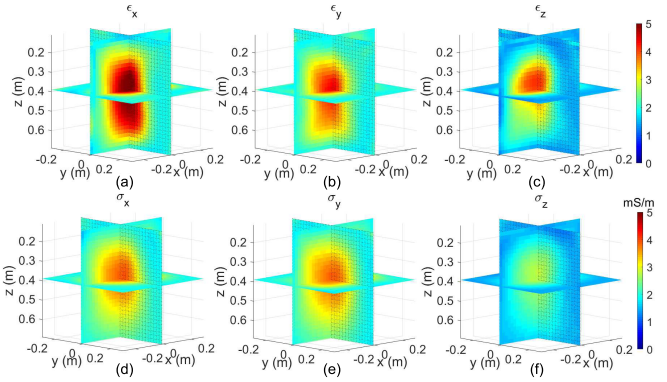

Fig. 3. Reconstructed 3-D profiles of the cuboid object by VBIM without SCC. (a)–(c) Relative permittivity and (d)–(f) conductivity.

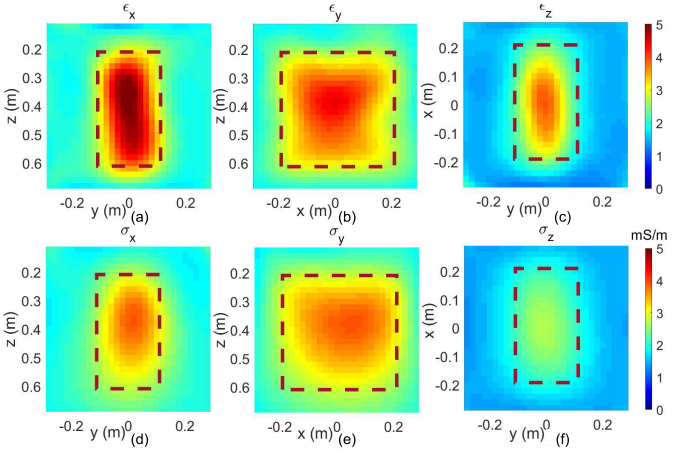

Fig. 4. 2-D slices of reconstructed results for the cuboid object by VBIM without SCC. (a) and (d) yz slices at $x = 0$ for reconstructed parameters of ε_x and σ_x, respectively. (b) and (e) xz slices at $y = 0$ for reconstructed parameters of ε_y and σ_y, respectively. (c) and (f) xy slices at $z = 0.4$ m for reconstructed parameters of ε_z and σ_z, respectively. The dotted boxes denote the true location and shape of the object.

For convenience, all transmitters are unit electric dipoles polarized in the direction of (1, 1, 1). The initial values of the unknowns are taken as the background parameters. In the previous work [1], [38], γ^2 is usually larger than 10^{-3}. Numerical simulations indicate that $\gamma = 0.05$ is an appropriate value in this work. Therefore, we set $\gamma^2 = 0.0025$ in all the numerical cases. The parameters in VBIM-SCC are set as $PreC = 5 \times 10^{-4}$, $N_1 = 4$, and $N_2 = 5$. The $PreC$ is chosen empirically since the previous work [25] shows that the reconstructed profiles are good enough when the threshold $PreC < 10^{-3}$. The selection of $PreT$ is referred to as a probability value following the normal distribution outside one variance and set to 15%. This is an appropriate value and is verified by all the numerical examples in this article. These configurations will not be repeated for each case in the following. The measured scattered data are synthesized by the forward BCGS-FFT solver with a finer mesh.

A. Cuboid Object Embedded in the Bottom Layer

A cuboid biaxial anisotropic object with a size of 0.4 m × 0.22 m × 0.4 m is embedded in the bottom layer, as shown in Fig. 2. The center of the object is located at $(0, -0.01, 0.4)$ m. The top layer is air. The relative permittivity and conductivity tensors are

$$\overline{\overline{\varepsilon}}_s = \text{diag}\{4, 3.5, 3\}, \quad \overline{\overline{\sigma}}_s = \text{diag}\{3.5, 4, 2.5\} \text{ mS/m} \quad (25)$$

for the scatterer and

$$\overline{\overline{\varepsilon}}_b^2 = \text{diag}\{2, 2, 1.5\}, \quad \overline{\overline{\sigma}}_b^2 = \text{diag}\{2, 2, 1.5\} \text{ mS/m} \quad (26)$$

for the bottom layer. The inversion domain enclosing the object has a dimension of 0.6 m × 0.6 m × 0.6 m, and its center is located at (0, 0, 0.4) m. The whole region is divided into 30^3 cells. The size of each cell is $\Delta x = \Delta y = \Delta z = 0.02$ m. The spatial sampling density of the discretization is around 50 points per wavelength (PPW) for the largest frequency and the largest relative permittivity value of the scatterer. We use this high PPW value only for the purpose of high reconstruction resolution. So, there are totally 162 000 unknowns to reconstruct. The transmitter array with 16 unit electric dipoles are uniformly located from 1.5 to 1.5 m at the $z = 0.1$ m plane. We choose five operating frequencies from 100 to 140 MHz with a step of 10 MHz. The scattered fields are collected by the receiver array with 36 dipoles uniformly located in a 1.8 m × 1.8 m square plane at $z = 0.05$ m. Thus, there are 34 560 data equations.

First, we perform the inversion by VBIM without SCC. After 35 iterations, the VBIM terminates with the RRE = 4.61×10^4. The reconstructed 3-D profiles are shown in Fig. 3 in which (a)–(c) represent the relative permittivity profiles and (d)–(f) represent the conductivity profiles. The 2-D slices are shown in Fig. 4. The yz slices at $x = 0$ for ε_x and σ_x are shown in Fig. 4(a) and (d), respectively. The 2-D xz slices at $y = 0$ and xy slices at $y = 0.4$ are shown in other four subfigures. The true location and shape of the object are shown in the dotted boxes. Compared with the true model, the locations are basically consistent, but the shapes cannot be clearly identified. The smooth edges of the reconstructed scatterers are caused by the L_2 norm Tikhonov-type regularization used in the cost function (20). And the retrieved model parameter values are roughly close to the true values.

For the same configuration, we perform the inversion by VBIM-SCC. The procedure terminates after 16 iterations with

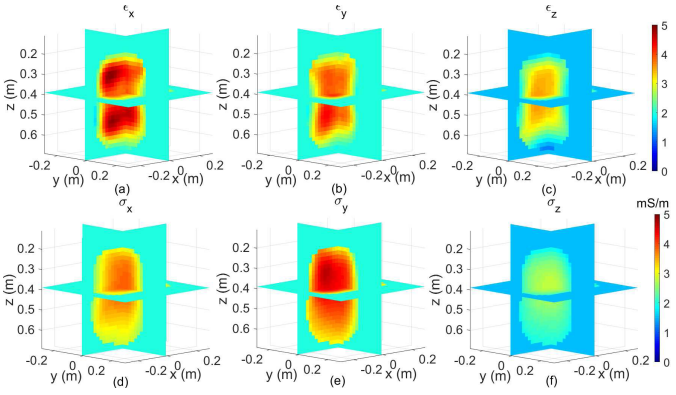

Fig. 5. Reconstructed 3-D profiles of the cuboid object by VBIM-SCC. (a)–(c) Relative permittivity and (d)–(f) Conductivity.

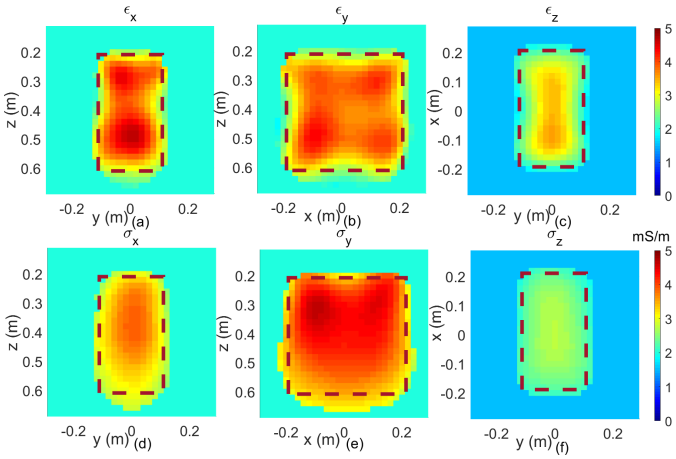

Fig. 6. 2-D slices of reconstructed results for the cuboid object by VBIM-SCC. (a) and (d) yz slices at $x = 0$ for reconstructed parameters of ε_x and σ_x, respectively. (b) and (e) xz slices at $y = 0$ for reconstructed parameters of ε_y and σ_y, respectively. (c) and (f) xy slices at $z = 0.4$ m for the reconstructed parameters of ε_z and σ_z, respectively.

RRE $= 4.45 \times 10^{-4}$. The results of 3-D profiles and 2-D slices are shown in Figs. 5 and 6, respectively. The slices shown in Fig. 6 are at the same locations as those in Fig. 4. Compared with the results of VBIM without SCC, both the location as well as the shape and the dielectric parameter values of the object are better reconstructed by the VBIM-SCC. We can see the existence of the trailing phenomenon at the bottom of the object by two methods. This is because all transmitters and receivers are placed on the top layer and the information at the bottom of the scatterer is not well reflected. Fortunately, VBIM-SCC mitigates the trailing phenomenon, but it cannot completely eliminate it. In order to evaluate the performance of inversion quantitatively, we define the model misfit as

$$\mathrm{Err}_{\mathrm{model}} = \frac{\|\mathbf{md}_R - \mathbf{md}_T\|}{\|\mathbf{md}_T\|} \tag{27}$$

where $\mathbf{md}_T$ is the true model parameter, and $\mathbf{md}_R$ is the reconstructed parameter. The model misfits for these two different VBIM schemes when iterations terminate are listed in Table I. VBIM-SCC has obviously lower model misfits for all retrieved parameters compared with VBIM without SCC.

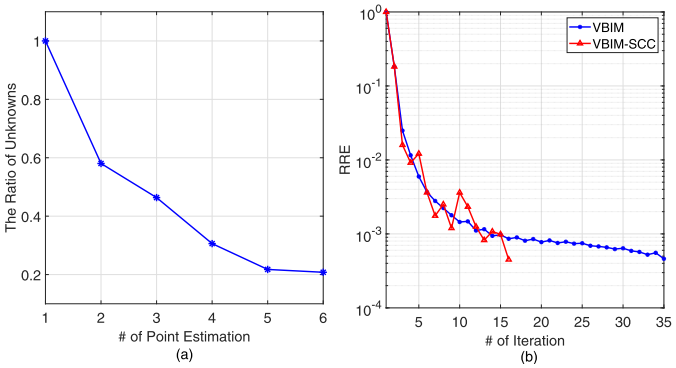

Fig. 7. Converging process of VBIM-SCC. (a) Ratio of unknowns after each point estimation. (b) RRE variations with VBIM iterations.

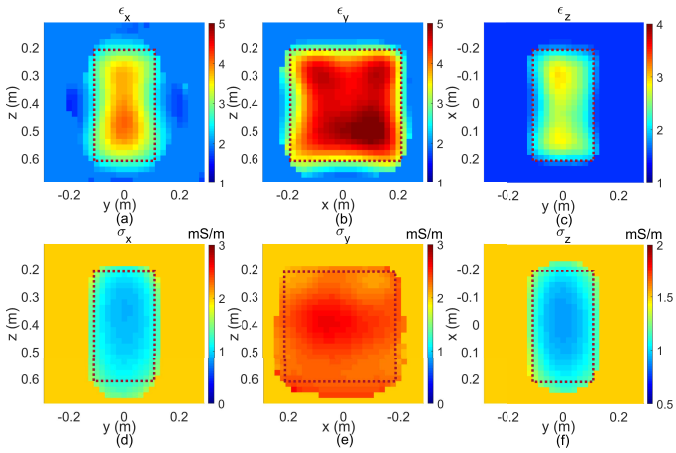

Fig. 8. 2-D slices of reconstructed results for different χ_{ar} values listed in Table II by VBIM-SCC. (a) ε_x in Group 1, (b) ε_y in Group 2, (c) ε_z in Group 3, (d) σ_x in Group 4, (e) σ_y in Group 5, and (f) σ_z in Group 6. The dotted boxes denote the true location and shape of the object.

TABLE I
MODEL MISFITS FOR VBIM WITH AND WITHOUT SCC

VBIM type	Model misfit(%)					
	ε_x	ε_y	ε_z	σ_x	σ_y	σ_z
VBIM	16.89	13.58	17.26	14.16	18.88	12.60
VBIM-SCC	13.25	10.57	12.42	10.67	13.50	9.86

When VBIM-SCC terminates, there are only 33 672 unknowns (5612 cells) for last point estimation which is far less than the total 162 000 unknowns (27 000 cells) in each iteration by VBIM without SCC. Fig. 7(a) shows the ratio of the remaining unknowns to the total unknowns after each point estimation, and Fig. 7(b) shows the RRE at each iteration for two methods. We can see that the number of unknowns is dramatically reduced by more than 40% after the first point estimation and then decreases steadily. This decrease not only helps save the computation time and memory but also lowers the total iteration steps, as shown in Fig. 7(b). Actually, it takes about 2 h to complete the inversion by VBIM-SCC, but 24 h by VBIM without SCC on the same workstation.

In order to investigate the performance of VBIM-SCC for different anisotropy, we define the degree of anisotropy of the

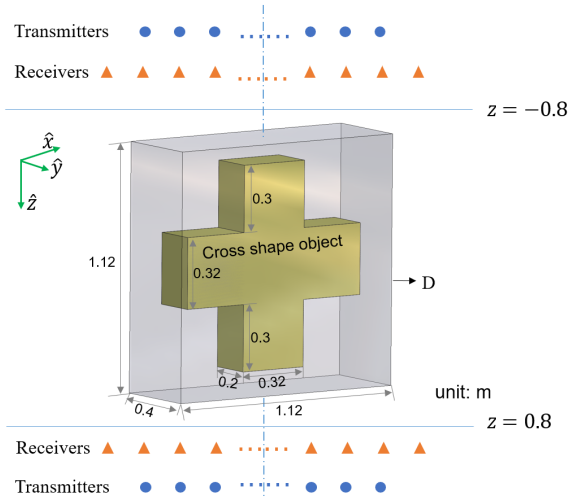

Fig. 9. Configuration of the inversion model with a cross shape scatterer embedded in the middle layer.

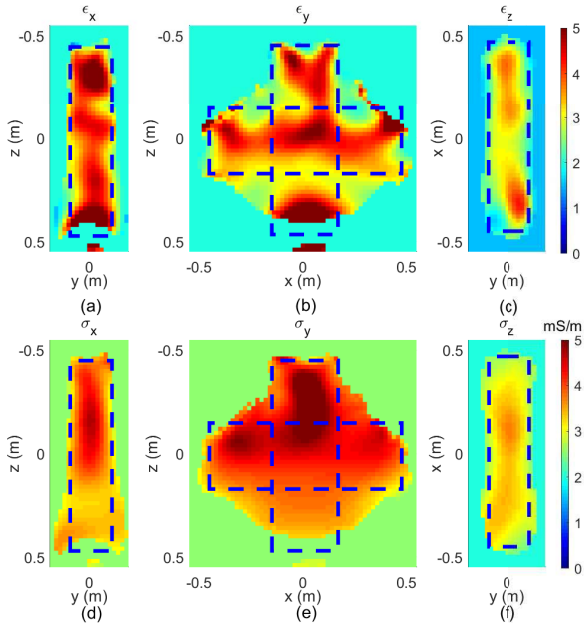

Fig. 10. 2-D slices of reconstructed results for the cross object in the first scenario. (a) and (d) yz slices at $x = 0$ for ε_x and σ_x, respectively. (b) and (e) xz slices at $y = 0$ for ε_y and σ_y, respectively. (c) and (f) xy slices at $z = 0$ for ε_z and σ_z, respectively.

complex contrast as [39]

$$\chi_{ar} = \frac{\sqrt{\sum_{j=1}^{M_F}\sum_{i=1}^{3}\|\chi_i(\omega_j) - \chi_{\text{ave}}\|^2}}{\sqrt{3 * M_F}\|\chi_{\text{ave}}\|} \tag{28}$$

where $\chi_i(\omega_j)$ with $i = 1, 2, 3$ are the diagonal elements of the contrast tensor $\overline{\overline{\chi}}(\omega_j) = \overline{\overline{\epsilon}}_s(\omega_j)/\overline{\overline{\epsilon}}_b(\omega_j) - 1$ for the jth frequency of the total M_F frequencies, and $\chi_{\text{ave}} = (\sum_{j=1}^{M_F}\sum_{i=1}^{3}\chi_i(\omega_j))/(3 * M_F)$.

We then test the VBIM-SCC algorithm for six different values of χ_{ar}, and the parameters are listed in Table II. One should note that we only change the anisotropic model parameters of the scatterers and keep those of the background medium the same as (26). The symbol MF_{ave} in Table II denotes the average model misfit of six reconstructed model parameters while ITEs are the total iteration number when VBIM-SCC terminates. The results show that as the degree of anisotropy increases from Group 1 to Group 6, the model misfit can roughly keep lower than 10% but more and more VBIM iterations are required to reach the same stop criterion. This means that the larger degree of anisotropy leads to higher computation cost for VBIM-SCC although the accuracy can be maintained. Fig. 8 shows the reconstructed profiles for six groups of parameters listed in Table II. Note only one parameter is displayed for one group. By comparing the results with those shown in Fig. 6, we can see that VBIM-SCC can reconstruct the anisotropic model parameters reliably even when the degree of anisotropy is very large.

Finally, one should note that both the memory and computation time costs of SCC are negligible compared with those of VBIM. This is because an iterative CG solver is used to solve the matrix (21) in each VBIM iteration, but the SCC only includes some arithmetical normalization or mean operations as shown in (23) and (24).

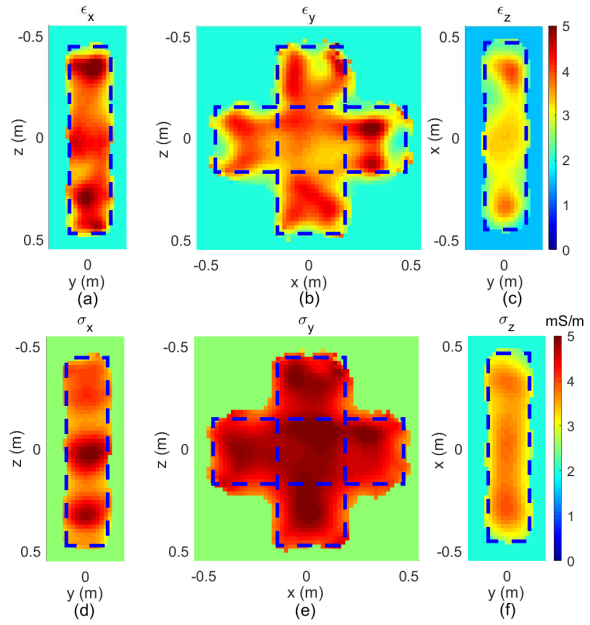

Fig. 11. 2-D slices of reconstructed results for the cross object in the second scenario. (a) and (d) yz slices at $x = 0$ for ε_x and σ_x, respectively. (b) and (e) xz slices at $y = 0$ for ε_y and σ_y, respectively. (c) and (f) xy slices at $z = 0$ for ε_z and σ_z, respectively.

TABLE II
DIFFERENT DEGREES OF ANISOTROPY USED TO TEST VBIM-SCC

Group	ε_x	ε_y	ε_z	σ_x	σ_y	σ_z	χ_{ar}	MF_{ave}	$ITEs$
1	3.5	2.5	2.5	2.5	3.5	2.5	0.39	8.53 %	9
2	3.5	4.0	1.0	4.0	3.5	1.0	1.23	10.16 %	12
3	3.5	1.0	2.5	1.0	3.5	2.5	1.87	9.92 %	17
4	3.0	1.0	1.0	1.0	3.0	1.0	3.94	7.53 %	17
5	2.5	1.0	2.0	1.0	2.5	1.0	13.49	6.07 %	22
6	3.5	1.0	1.0	1.0	3.5	1.0	19.95	8.78 %	22

Remark: the unit of σ is mS/m.

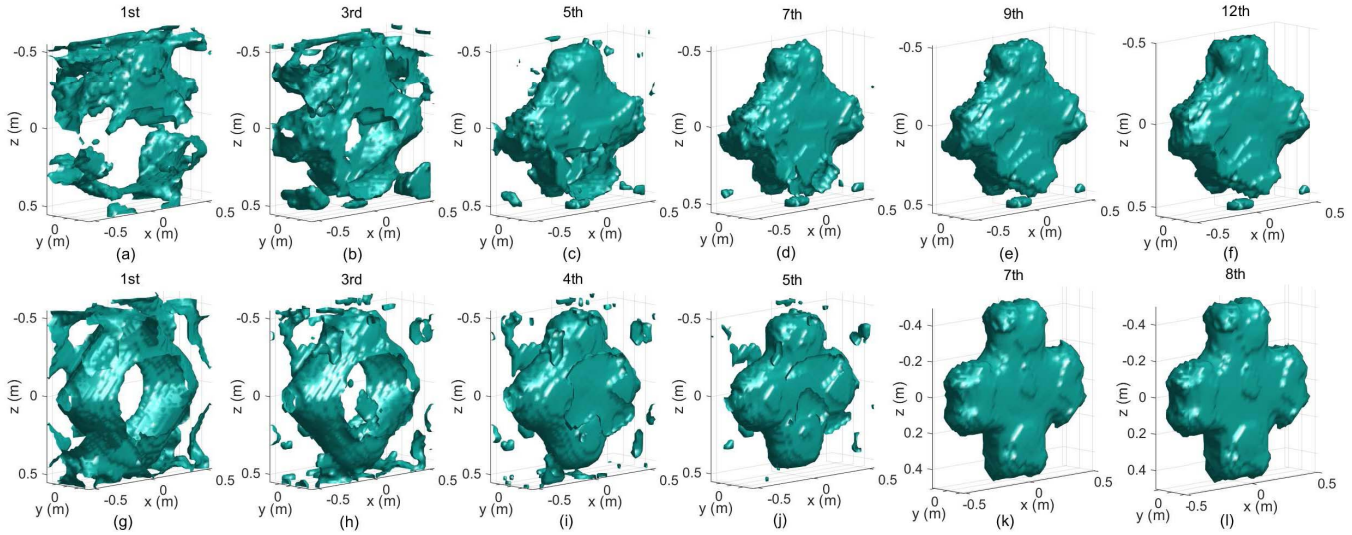

Fig. 12. Structure focusing processes in two different scenarios by VBIM-SCC are shown from left to right. The structure snapshots of (a)–(f) are taken in the 1st, 3rd, 5th 7th, 9th, and the last point estimation for the first scenario and (g)–(l) are taken in the 1st, 3rd, 4th, 5th, 7th, and the last point estimation for the second scenario.

B. Cross Shape Object Embedded in the Middle Layer

In this case, we investigate the reconstruction of a cross shape object. As shown in Fig. 9, the top layer and the bottom layer are air. A cross shape object is embedded in the middle layer. The centers of both the object and the inversion domain are located at the origin. The sizes of the object and reconstruction region are shown in Fig. 9. The whole inversion domain is divided into $56 \times 20 \times 56$ cells and the size of each cell is $\Delta x = \Delta y = \Delta z = 0.02$ m. So, there are totally 376 320 unknowns to reconstruct. The relative permittivity and conductivity tensors are given as

$$\overline{\overline{\varepsilon}}_s = \text{diag}\{4, 3.5, 3\}, \quad \overline{\overline{\sigma}}_s = \text{diag}\{4, 4.5, 3.5\} \text{ mS/m} \quad (29)$$

for the cross shape object, and

$$\overline{\overline{\varepsilon}}_b^2 = \text{diag}\{2, 2, 1.5\}, \quad \overline{\overline{\sigma}}_b^2 = \text{diag}\{2.5, 2.5, 2\} \text{ mS/m} \quad (30)$$

for the middle layer.

We inspect the proposed VBIM-SCC for two scenarios. In the first scenario, the cross-shape object is illuminated by transmitter and receiver arrays placed on one side of the inversion domain. In the second scenario, they are placed on two sides. A 5×3 transmitter array and a 9×4 receiver array are employed in the first scenario. The transmitters are uniformly placed in a 2 m $\times$ 1.2 m rectangular area at the $z = -0.9$ m plane. The receivers are uniformly placed in a 3.6 m $\times$ 1.8 m rectangular area at the $z = -0.85$ m plane. In the second scenario, the transmitter array and the receiver array are 3×3 and 4×4, respectively. However, two identical transmitter arrays and receiver arrays are placed on both the top and bottom layers. Their positions and spatial sizes are the same as those in the first scenario. Four operation frequencies from 100 to 160 MHz with the step of 20 MHz are chosen. The numbers of data equations are the same for two scenarios. The procedure of VBIM-SCC terminates after 51 iterations with RRE $= 4.73 \times 10^{-4}$ in the first scenario and 31 iterations with RRE $= 4.69 \times 10^{-4}$ in the second scenario. The 2-D slices are shown in Fig. 10 for the first scenario and Fig. 11 for the second scenario, respectively. Also, the dotted boxes show the true location and shape of the cross shape object. Compared with the true cross shape model, we can see that not only the position and shape of the object but also the model parameters are better reconstructed in the second scenario. Another interesting observation is the arc shape showing up at the bottom of the reconstructed xz slices in the first scenario. This phenomenon disappears in the second scenario. This is similar to the trailing phenomenon discussed in the last case. Since the transmitter and receiver arrays are placed only on the top layer in the first scenario, the bottom information of the cross-shape object is not well reflected. When the bottom shape is distorted in the reconstruction, the top shape will also become bad even when we place enough transmitters and receivers in the top layer. The only way to improve the reconstructed results is to increase the array aperture, e.g., put the transmitter and receiver arrays in two sides of the object. And this is illustrated by the results shown in Fig. 11.

The main contribution of SCC is to constrain and accelerate the focusing process of the reconstructed structures. Fig. 12 shows the focusing processes of the reconstructed structures in two scenarios. Each snapshot represents the reconstructed structure after a certain point estimation. Clearly, SCC works better for the two-side illumination.

C. Three Objects Embedded in the Bottom Layer

Due to the L_2 norm used in the cost function of VBIM, the cubic scatterers tend to be reconstructed as spheres [40]. Fortunately, SCC can effectively improve this deficiency. In this case, we inspect the inversion for multiple cubic objects embedded in the bottom layer with different dielectric parameters to mimic cross-well measurements. The top layer is air. We put all the transmitters and receivers inside boreholes in the bottom layer, and noise at different levels is added to

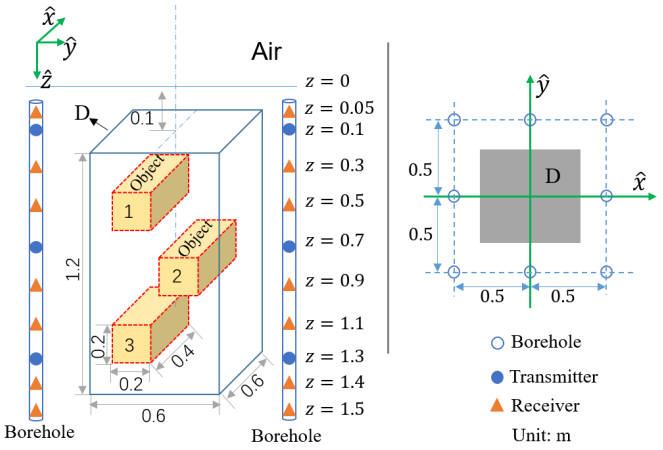

Fig. 13. Cross-well model. The left part is the illustration of the model and the right part is the location sketch of the boreholes in the xy-plane.

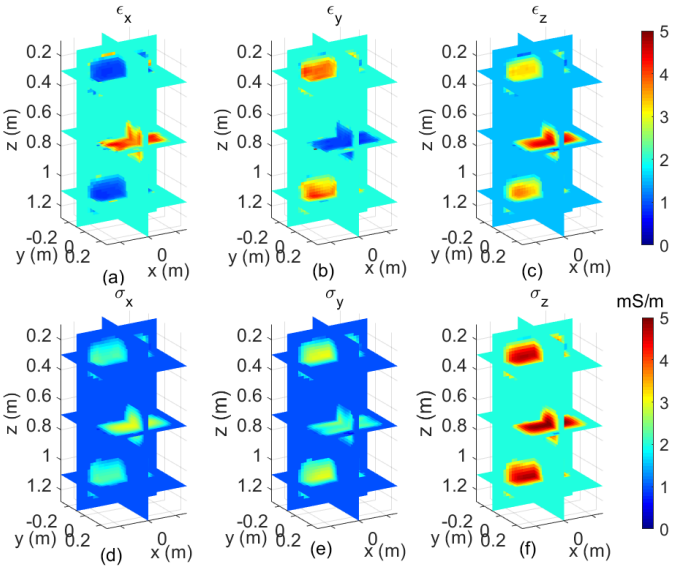

Fig. 14. Reconstructed 3-D profiles for three objects by VBIM-SCC. (a)–(c) for the relative permittivity and (d)–(f) for the conductivity.

the simulated data. The inversion model is shown in Fig. 13. In the left part, three rectangular objects with the dimension of 0.4 m × 0.2 m × 0.2 m are investigated. The centers of three objects are $(0, -0.1, 0.25)$ m, $(0, 0.1, 0.7)$ m and $(0, -0.1, 1.1)$ m, respectively. The relative permittivity and conductivity tensors are given as

$$\overline{\overline{\varepsilon}}_{s1} = \text{diag}\{1.0, 3.5, 3.0\}, \quad \overline{\overline{\sigma}}_{s1} = \text{diag}\{2, 2.5, 4\} \text{ mS/m} \quad (31)$$

for the first and the third object, and

$$\overline{\overline{\varepsilon}}_{s2} = \text{diag}\{3.5, 1.0, 3.5\}, \quad \overline{\overline{\sigma}}_{s2} = \text{diag}\{2.5, 2, 4\} \text{ mS/m} \quad (32)$$

for the second object. The background model parameters of the bottom layer are given as

$$\overline{\overline{\varepsilon}}_b^2 = \text{diag}\{2.0, 2.0, 1.5\}, \quad \overline{\overline{\sigma}}_b^2 = \text{diag}\{1, 1, 2\} \text{ mS/m} \quad (33)$$

the same as those for the first case. The inversion domain has the dimensions of 0.6 m × 0.6 m × 1.2 m and its center is located at $(0, 0, 0.7)$ m. The region is divided into

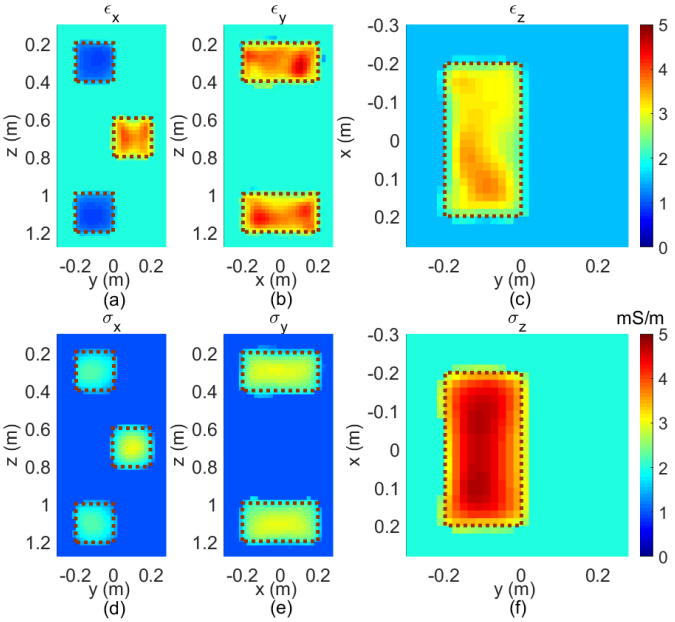

Fig. 15. 2-D slices of reconstructed results for three objects by VBIM-SCC. (a) and (d) yz slices at $x = 0$ for reconstructed parameters of ε_x and σ_x, respectively. (b) and (e) xz slices at $y = -0.06$ m for reconstructed parameters of ε_y and σ_y, respectively. (c) and (f) xy slices at $z = 0$ for reconstructed parameters of ε_z and σ_z, respectively.

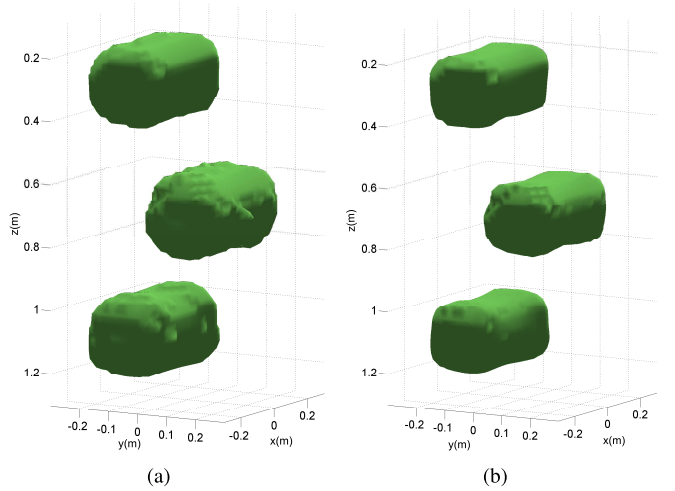

Fig. 16. 3-D isosurface plots of the reconstructed shape. (a) Isosurface for $\mathbf{P}_6 = 15\%$. (b) Isosurface for $\mathbf{P}_6 = 30\%$.

$30 \times 30 \times 60$ cells. The size of each cell is $\Delta x = \Delta y = \Delta z = 0.02$ m. Thus, there are 324 thousand unknowns to solve. Seven receivers and three transmitters are placed in each borehole. Eight boreholes are drilled around the reconstruction region, and the locations are shown on the right panel of Fig. 13. Five operation frequencies are chosen from 80 to 120 MHz with a step of 10 MHz.

After 17 iterations, the VBIM-SCC terminates with RRE $= 4.82 \times 10^{-4}$. The reconstructed 3-D profiles of the relative permittivity and conductivity are shown in Fig. 14. The 2-D slices are shown in Fig. 15. We can see that not only the locations and shapes but also the model parameter values are all well reconstructed. And there are only 49 050 unknowns (8175 cells) to invert for after the last point estimation.

TABLE III

MISFITS FOR DIFFERENT LEVELS OF NOISE CONTAMINATION IN THE CROSS-WELL MODEL OF THREE RECTANGULAR OBJECTS

Misfit \ SNR		Noise-free	20 dB	30 dB	40 dB
Data misfit(%)	**E** field	0.050	9.90	3.15	1.00
	H field	0.047	9.96	3.14	1.00
Model misfit(%)	ε_x	7.16	12.10	9.21	7.90
	ε_y	20.50	22.64	21.37	20.60
	ε_z	11.93	17.56	13.93	13.44
	σ_x	12.85	18.06	15.07	14.28
	σ_y	14.26	19.67	16.60	15.65
	σ_z	11.16	15.77	13.18	12.13

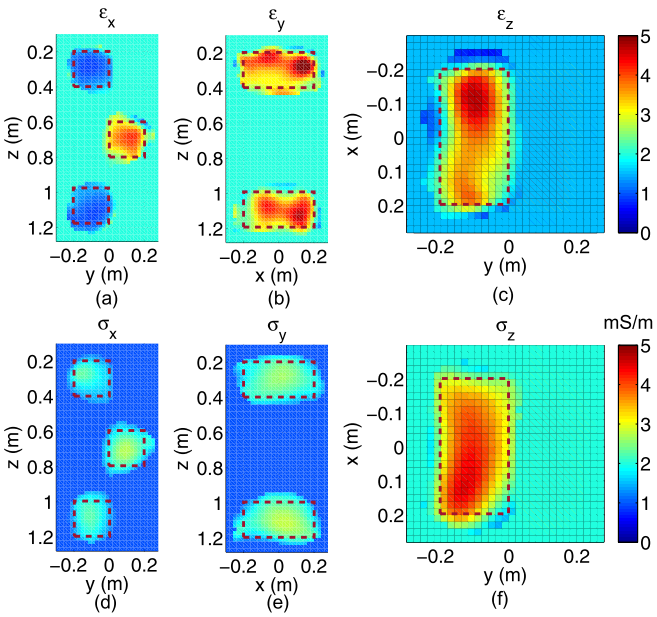

Fig. 17. 2-D slices of reconstructed results for three objects when SNR = 20 dB by VBIM-SCC. (a) and (d) yz slices at $x = 0$ for reconstructed parameters of ε_x and σ_x, respectively. (b) and (e) xz slices at $y = -0.06$ m for reconstructed parameters of ε_y and σ_y, respectively. (c) and (f) Are xy slices at $z = 0$ for reconstructed parameters of ε_z and σ_z, respectively.

Because transmitters and receivers wrap the inversion domain, the trailing phenomenon does not show up.

The point estimation is performed six times when the 17 iterations terminate. Fig. 16 shows the 3-D isosurface plots of the reconstructed shapes for the last point estimation when the inversion ends. The isosurface for $\mathbf{P}_6 = PreT$ (15%) is shown in (a) and for $\mathbf{P}_6 = 30\%$ is shown in (b) in Fig. 16. In (a), it is observed that three scatterers are clearly separated and their locations and shapes can be identified. Thus, the SCC algorithm also has a good structural constraint for multiple objects. When $\mathbf{P}_6 = 30\%$, the isosurface becomes smoother and closer to the true model than when $\mathbf{P}_6 = 15\%$. The constraint of structural consistency is relaxed to avoid deleting the cell of "scatterer" by mistake.

To simulate realistic measurements and test the antinoise ability of VBIM-SCC, we add the white Gaussian noise to the simulated scattered field to form synthetic data. We set the power signal-to-noise ratio (SNR) of the synthetic data as 20, 30, and 40 dB, respectively. Thus, the ratios between noise and the signal amplitudes are about 10%, 3.16%, and 1%, respectively. When RRE reduces to 11.33%, 3.63%, and 1.14% for SNR = 20, 30, and 40 dB, respectively, it remains unchanged and VBIM-SCC inversion procedures terminate. The 2-D slices of the reconstructed results for SNR = 20 dB are shown in Fig. 17. The reconstructed objects are at the same locations as those shown in Fig. 15. Although the shapes are distorted to some extent, the multiple objects are clearly distinguishable and the retrieved parameter values are close to the true values. The reconstructed results for SNR = 30 and 40 dB are not shown, but the results are better than those for SNR = 20 dB. We define the data misfit as

$$\mathrm{Err}_{\mathrm{data}} = \frac{\|\mathbf{da}_R - \mathbf{da}_T\|}{\|\mathbf{da}_T\|} \tag{34}$$

where $\mathbf{da}_T$ is the measured scattered field and $\mathbf{da}_R$ is the reconstructed scattered field. The data misfits and model misfits for the noise-free model and noisy models are calculated and listed in Table III. We can see that data misfits are close to the amplitude SNR values, and model misfits for SNR = 40 dB are close to those for the noise-free model. Thus, the VBIM-SCC has a certain antinoise ability.

IV. CONCLUSION

In this article, we present the EM inversion of 3-D biaxial anisotropic objects embedded in layered uniaxial media by VBIM when the optical axes are all aligned with the direction perpendicular to the layer interfaces. The data equation for multifrequency measured fields is formulated and rewritten in the real form. Thus, both permittivity and conductivity can be reconstructed simultaneously. The SCC algorithm based on the Monte Carlo method is developed to accelerate VBIM and improve reconstructed results by reducing the reconstruction region in each iteration.

Three numerical examples are simulated to validate the performance of the proposed inversion method. The objects in all three cases are well reconstructed by the VBIM-SCC method. Compared with the VBIM without SCC, the VBIM-SCC method saves both the computation time and memory by reducing the reconstruction region in each iteration. Meanwhile, the quality of the reconstructed objects is obviously improved, which is validated by the comparisons of model misfits. When the apertures of the transmitter and receiver arrays are increased, VBIM-SCC performs better. And this is shown in the second numerical case. The inversion capability of multiple objects with different dielectric parameters shows the potential applications of our method in cross-well explorations. The reconstruction at different noise levels shows that the VBIM-SCC method has a certain antinoise ability.

For the first time, we combine the deterministic inversion method VBIM with the stochastic Monte Carlo method. Although this is the first attempt and only the numerical examples are presented to mimic the real-world measurement scenarios, the performance of the inversion is improved obviously and its effectiveness is also validated. The proposed hybrid VBIM-SCC provides a new way of solving the EM inverse scattering problems. As we know, the EM inversion methods fall into two categories. One is the deterministic inversion

and the other one is the stochastic inversion. In the deterministic inversion, the dimension of model parameters has no restriction. This is specifically powerful for 3-D voxel-based inversion, i.e., the model parameters in all discretized cells are reconstructed simultaneously. However, iterative solvers, e.g., VBIM are easily trapped in local minima and the solution is not necessarily the most optimized one since the inverse scattering problems are usually underdetermined. By contrast, the stochastic methods search the optimized solutions randomly and can avoid being trapped into local minima. Unfortunately, the dimension of unknowns is severely restricted, which is problematic for the 3-D voxel-based inversion in which the model parameters in all discretized cells must be retrieved. The VBIM-SCC in this article is first utilizing the Monte Carlo method to reconstruct the structures of scatterers using the statistical data of model parameters in all discretized cells. Consequently, the inversion domain is compressed and the underdetermination of the inverse problem is mitigated. This facilitates the deterministic solver to rapidly reach the optimal solutions.

One should note that the SCC proposed in this article is combined with VBIM, but it is not only limited to VBIM. It can be easily combined with any voxel-based deterministic inversion algorithms such as SOM or CSI as long as the sampling space is large enough. The future work will be focused on two aspects. One is the combination of the VBIM with artificial intelligence technology such as deep learning or a convolutional neural network. The other one is the validation of the proposed hybrid method in the laboratory experiments. Several issues must be considered. First, the EM wave scattering by measurement instruments or laboratory surroundings must be considered. Second, the transmitter and receiver antenna arrays are not allowed to be uniquely polarized. Versatile polarization is necessary since some components of the anisotropic dielectric parameter tensors are not sensitive to the change of vertical electric fields. Third, the construction of the layered uniaxial background media is not easy. One possible solution is to use thin isotropic slabs stacked periodically. However, such an experiment is too challenging at the current stage and will be left as our future research work.

REFERENCES

[1] T. Lan, N. Liu, Y. Liu, F. Han, and Q. H. Liu, "2-D electromagnetic scattering and inverse scattering from magnetodielectric objects based on integral equation method," *IEEE Trans. Antennas Propag.*, vol. 67, no. 2, pp. 1346–1351, Feb. 2019.

[2] Y. Hu, Y. Fang, D. Labrecque, M. Ahmadian, and Q. H. Liu, "Reconstruction of high-contrast proppant in hydraulic fractures with galvanic measurements," *IEEE Trans. Geosci. Remote Sens.*, vol. 56, no. 4, pp. 2066–2073, Apr. 2018.

[3] R. Hong *et al.*, "3-D MRI-Based electrical properties tomography using the volume integral equation method," *IEEE Trans. Microw. Theory Tech.*, vol. 65, no. 12, pp. 4802–4811, Dec. 2017.

[4] M. Hunter *et al.*, "Tissue self-affinity and polarized light scattering in the Born approximation: A new model for precancer detection," *Phys. Rev. Lett.*, vol. 97, no. 13, p. 138102, Sep. 2006.

[5] H. Liu, Z. Deng, F. Han, Y. Xia, Q. H. Liu, and M. Sato, "Time-frequency analysis of air-coupled GPR data for identification of delamination between pavement layers," *Construct. Building Mater.*, vol. 154, pp. 1207–1215, Nov. 2017.

[6] G. L. Wang, T. Barber, P. Wu, D. Allen, and A. Abubakar, "Fast inversion of triaxial induction data in dipping crossbedded formations," *Geophysics*, vol. 82, no. 2, pp. D31–D45, Mar. 2017.

[7] J. Pek and F. A. Santos, "Magnetotelluric inversion for anisotropic conductivities in layered media," *Phys. Earth Planet. Interiors*, vol. 158, nos. 2–4, pp. 139–158, Oct. 2006.

[8] V. Sesetty and A. Ghassemi, "Effect of rock anisotropy on wellbore stresses and hydraulic fracture propagation," *Int. J. Rock Mech. Mining Sci.*, vol. 112, pp. 369–384, Dec. 2018.

[9] R. W. Deming and A. J. Devaney, "Diffraction tomography for multi-monostatic ground penetrating radar imaging," *Inverse Problems*, vol. 13, no. 1, pp. 29–45, Feb. 1997.

[10] L. Poli, G. Oliveri, and A. Massa, "Microwave imaging within the first-order born approximation by means of the contrast-field Bayesian compressive sensing," *IEEE Trans. Antennas Propag.*, vol. 60, no. 6, pp. 2865–2879, Jun. 2012.

[11] P.-A. Barriere, J. Idier, Y. Goussard, and J.-J. Laurin, "Fast solutions of the 2D inverse scattering problem based on a TSVD approximation of the internal field for the forward model," *IEEE Trans. Antennas Propag.*, vol. 58, no. 12, pp. 4015–4024, Dec. 2010.

[12] A. Abubakar, P. M. Van den Berg, and J. J. Mallorqui, "Imaging of biomedical data using a multiplicative regularized contrast source inversion method," *IEEE Trans. Microw. Theory Tech.*, vol. 50, no. 7, pp. 1761–1771, Jul. 2002.

[13] C. Gilmore, P. Mojabi, and J. Lovetri, "Comparison of an enhanced distorted born iterative method and the multiplicative-regularized contrast source inversion method," *IEEE Trans. Antennas Propag.*, vol. 57, no. 8, pp. 2341–2351, Aug. 2009.

[14] A. Zakaria, C. Gilmore, and J. Lovetri, "Finite-element contrast source inversion method for microwave imaging," *Inverse Problems*, vol. 26, no. 11, Nov. 2010, Art. no. 115010.

[15] X. Chen, "Subspace-based optimization method for solving inverse-scattering problems," *IEEE Trans. Geosci. Remote Sens.*, vol. 48, no. 1, pp. 42–49, Jan. 2010.

[16] K. Agarwal, L. Pan, and X. Chen, "Subspace-based optimization method for reconstruction of 2-D complex anisotropic dielectric objects," *IEEE Trans. Microw. Theory Techn.*, vol. 58, no. 4, pp. 1065–1074, Apr. 2010.

[17] Y. Liu *et al.*, "A frequency-hopping subspace-based optimization method for reconstruction of 2-D large uniaxial anisotropic scatterers with TE illumination," *IEEE Trans. Geosci. Remote Sens.*, vol. 54, no. 10, pp. 6091–6099, Oct. 2016.

[18] Y. Zhong, M. Lambert, D. Lesselier, and X. Chen, "A new integral equation method to solve highly nonlinear inverse scattering problems," *IEEE Trans. Antennas Propag.*, vol. 64, no. 5, pp. 1788–1799, May 2016.

[19] Y. M. Wang and W. C. Chew, "An iterative solution of the two-dimensional electromagnetic inverse scattering problem," *Int. J. Imag. Syst. Technol.*, vol. 1, no. 1, pp. 100–108, 1989.

[20] W. C. Chew and Y. Wang, "Reconstruction of two-dimensional permittivity distribution using the distorted Born iterative method," *IEEE Trans. Med. Imag.*, vol. 9, no. 2, pp. 218–225, Jun. 1990.

[21] Q. H. Liu, "Nonlinear inversion of electrode-type resistivity measurements," *IEEE Trans. Geosci. Remote Sens.*, vol. 32, no. 3, pp. 499–507, May 1994.

[22] C. Yu, M. Yuan, and Q. H. Liu, "Reconstruction of 3D objects from multi-frequency experimental data with a fast DBIM-BCGS method," *Inverse Problems*, vol. 25, no. 2, Feb. 2009, Art. no. 024007.

[23] W. Zhang, L. Li, and F. Li, "Multifrequency imaging from intensity-only data using the phaseless data distorted Rytov iterative method," *IEEE Trans. Antennas Propag.*, vol. 57, no. 1, pp. 290–295, Jan. 2009.

[24] Z. Nie, F. Yang, Y. Zhao, and Y. Zhang, "Variational born iteration method and its applications to hybrid inversion," *IEEE Trans. Geosci. Remote Sens.*, vol. 38, no. 4, pp. 1709–1715, Jul. 2000.

[25] W. Zhang and Q. H. Liu, "Three-dimensional scattering and inverse scattering from objects with simultaneous permittivity and permeability contrasts," *IEEE Trans. Geosci. Remote Sens.*, vol. 53, no. 1, pp. 429–439, Jan. 2015.

[26] H. Harada, D. Wall, T. Takenaka, and M. Tanaka, "Conjugate gradient method applied to inverse scattering problem," *IEEE Trans. Antennas Propag.*, vol. 43, no. 8, pp. 784–792, Aug. 1995.

[27] P. Mojabi and J. Lovetri, "Overview and classification of some regularization techniques for the Gauss–Newton inversion method applied to inverse scattering problems," *IEEE Trans. Antennas Propag.*, vol. 57, no. 9, pp. 2658–2665, Sep. 2009.

[28] Y. Zhong and X. Chen, "MUSIC imaging and electromagnetic inverse scattering of multiple-scattering small anisotropic spheres," *IEEE Trans. Antennas Propag.*, vol. 55, no. 12, pp. 3542–3549, Dec. 2007.
[29] L.-P. Song, Q. H. Liu, F. Li, and Z. Q. Zhang, "Reconstruction of three-dimensional objects in layered media: Numerical experiments," *IEEE Trans. Antennas Propag.*, vol. 53, no. 4, pp. 1556–1561, Apr. 2005.
[30] F. Han, J. Zhuo, N. Liu, Y. Liu, H. Liu, and Q. H. Liu, "Fast Solution of electromagnetic scattering for 3-D inhomogeneous anisotropic objects embedded in layered uniaxial media by the BCGS-FFT method," *IEEE Trans. Antennas Propag.*, vol. 67, no. 3, pp. 1748–1759, Mar. 2019.
[31] C. A. Balanis, Ed., *Advanced Engineering Electromagnetics*. New York, NY, USA: Wiley, 1989.
[32] W. C. Chew, *Waves and Fields in Inhomogeneous Media*. New York, NY, USA: Van Nostrand Reinhold, 1990.
[33] K. Michalski and J. Mosig, "Multilayered media Green's functions in integral equation formulations," *IEEE Trans. Antennas Propag.*, vol. 45, no. 3, pp. 508–519, Mar. 1997.
[34] C. L. Lawson and R. J. Hanson, Eds., *Solving Least Squares Problems*. Englewood Cliffs, NJ, USA: Prentice-Hall, 1974.
[35] M. F. Catedra, R. P. Torres, J. Basterrechea, and E. Gago, Eds., *CG-FFT Method: Application of Signal Processing Techniques to Electromagnetics*. Boston, MA, USA: Artech House, 1994.
[36] M. Commer and G. A. Newman, "New advances in three-dimensional controlled-source electromagnetic inversion," *Geophys. J. Int.*, vol. 172, no. 2, pp. 513–535, Feb. 2008.
[37] A. Tarantola, Ed., *Inverse Problem Theory and Methods for Model Parameter Estimation*. Philadelphia, PA, USA: SIAM, 2005.
[38] B. Liang *et al.*, "A new inversion method based on distorted born iterative method for grounded electrical source airborne transient electromagnetics," *IEEE Trans. Geosci. Remote Sens.*, vol. 56, no. 2, pp. 877–887, Feb. 2018.
[39] G. Oliveri, E. T. Bekele, M. Salucci, and A. Massa, "Transformation electromagnetics miniaturization of sectoral and conical metamaterial-enhanced horn antennas," *IEEE Trans. Antennas Propag.*, vol. 64, no. 4, pp. 1508–1513, Apr. 2016.
[40] Y. Chen, P. Wen, F. Han, N. Liu, H. Liu, and Q. H. Liu, "Three-dimensional reconstruction of objects embedded in spherically layered media using variational born iterative method," *IEEE Geosci. Remote Sens. Lett.*, vol. 14, no. 7, pp. 1037–1041, Jul. 2017.

Jianliang Zhuo received the B.S. degree in communication engineering and business administration and the M.S. degree in communication and information system from the University of Electronic Science and Technology of China, Chengdu, China, in 2007 and 2011, respectively, and the Ph.D. degree in physical electronics from Xiamen University, Xiamen, China, in 2018.

Since 2018, he has been a Post-Doctoral Fellow of the postdoctoral mobile station of information and communication engineering with Xiamen University. His research interests include fast forward solvers in electromagnetics and inverse scattering methods for microelectronics and RF systems.

Longfang Ye received the Ph.D. degree in electromagnetic field and microwave technology from the University of Electronic Science and Technology of China, Chengdu, China, in 2013.

From October 2011 to January 2013, he was a Visiting Student with the Massachusetts Institute of Technology, Cambridge, MA, USA. Since July 2013, he has been an Assistant Professor with the Department of Electronic Science, Institute of Electromagnetics and Acoustics, Xiamen University, Xiamen, China. His current research interests include microwave circuits and antennas, terahertz waveguides, and graphene-based devices.

Feng Han (Member, IEEE) received the B.S. degree in electronic science from Beijing Normal University, Beijing, China, in 2003, the M.S. degree in geophysics from Peking University, Beijing, in 2006, and the Ph.D. degree in electrical engineering from Duke University, Durham, NC, USA, in 2011.

He is currently an Assistant Professor with the Institute of Electromagnetics and Acoustics, Xiamen University, Xiamen, China. His research interests include ionosphere remote sensing by radio atmospherics, electromagnetic full-wave inversion by integral equations, reverse time migration image, and the design of an electromagnetic detection system.

Liujing Xiong received the B.S. degree in mechanical design, manufacturing, and automation from the Hefei University of Technology, Hefei, China, in 2010, and the M.S. degree from the Institute of Electromagnetics and Acoustics, Xiamen University, Xiamen, China, in 2015.

Since 2015, she has been an Engineer with the Institute of Electromagnetics and Acoustics, Xiamen University. Her current research interests include planar antenna design and electromagnetic inverse scattering.

Qing Huo Liu (Fellow, IEEE) received the B.S. and M.S. degrees in physics from Xiamen University, Xiamen, China, and the Ph.D. degree in electrical engineering from the University of Illinois at Urbana–Champaign, Champaign, IL, USA.

He was a Research Assistant with the Electromagnetics Laboratory, University of Illinois at Urbana–Champaign, from September 1986 to December 1988, and a Post-Doctoral Research Associate from January 1989 to February 1990. From 1990 to 1995, he was a Research Scientist and the Program Leader with Schlumberger-Doll Research, Ridgefield, CT, USA. From 1996 to May 1999, he was an Associate Professor with New Mexico State University, Las Cruces, NM, USA. Since June 1999, he has been with Duke University, Durham, NC, USA, where he is currently a Professor of electrical and computer engineering. Since 2005, he has been the Founder and the Chairman of Wave Computation Technologies, Inc. His research interests include computational electromagnetics and acoustics, inverse problems, and their application in nanophotonics, geophysics, biomedical imaging, and electronic packaging. He has published widely in these areas.

Dr. Liu is a fellow of the Acoustical Society of America, the Electromagnetics Academy, and the Optical Society of America. He has served as an IEEE Antennas and Propagation Society Distinguished Lecturer and the Founding Editor-in-Chief for the IEEE JOURNAL ON MULTISCALE AND MULTIPHYSICS COMPUTATIONAL TECHNIQUES. He received the 1996 Presidential Early Career Award for Scientists and Engineers (PECASE) from the White House, the 1996 Early Career Research Award from the Environmental Protection Agency, the 1997 CAREER Award from the National Science Foundation, the 2017 Technical Achievement Award, the 2018 Computational Electromagnetics Award from the Applied Computational Electromagnetics Society, the 2018 Harrington-Mittra Award in Computational Electromagnetics from the IEEE Antennas and Propagation Society, and the ECE Distinguished Alumni Award from the University of Illinois at Urbana–Champaign in 2018.